

# A spatial transcriptome map of developing maize ear

**Ning Yang**

ningyu@mail.hzau.edu.cn

Huazhong Agricultural University

**Yuebin Wang**

Huazhong Agricultural University

**Yun Luo**

Huazhong Agricultural University

**Xing Guo**

BGI-Shenzhen

**Yunfu Li**

Huazhong Agricultural University <https://orcid.org/0000-0002-9468-5981>

**Jiali Yan**

Huazhong Agricultural University <https://orcid.org/0000-0003-0295-6594>

**Wenwen Shao**

BGI-Shenzhen

**Wenjie Wei**

Huazhong Agricultural University

**David Jackson**

Cold Spring Harbor Laboratory <https://orcid.org/0000-0002-4269-7649>

**Zuxin Zhang**

Huazhong Agricultural University <https://orcid.org/0000-0001-8697-1681>

**Jianbing Yan**

Huazhong Agricultural University <https://orcid.org/0000-0001-8650-7811>

**Huan Liu**

BGI-Shenzhen, Shenzhen 518083, China <https://orcid.org/0000-0003-3909-0931>

**Lei Liu**

Huazhong Agricultural University



---

**Article**

**Keywords:**

**Posted Date:** June 24th, 2023

**DOI:** <https://doi.org/10.21203/rs.3.rs-3037245/v1>

**License:**   This work is licensed under a Creative Commons Attribution 4.0 International License. [Read Full License](#)

**Additional Declarations:** There is **NO** Competing Interest.

---

**Version of Record:** A version of this preprint was published at Nature Plants on May 14th, 2024. See the published version at <https://doi.org/10.1038/s41477-024-01683-2>.

# Abstract

A comprehensive understanding of inflorescence development is crucial for crop genetic improvement, as inflorescence meristems give rise to reproductive organs and determine grain yield. However, dissecting inflorescence development at the cellular level has been challenging due to the lack of distinct marker genes to distinguish each cell types, particularly the various types of meristems that are vital for organ formation. In this study, we used spatial enhanced resolution omics-sequencing (Stereo-seq) to construct a precise spatial transcriptome map of developing maize ear primordia, identifying twelve cell types, including the four newly cell types that mainly distributed on inflorescence merisetm. Through integrating single-cell RNA transcriptomes, we identified a series of spatially-specific networks and hub genes, which may provide new insights on understanding the formation of different tissues. Furthermore, by extracting the meristem components for detailed clustering, we identified three subtypes of meristem, and validated two MADS-box genes specifically expressed at the apex of determinate meristems, involved in stem cell determinacy. In summary, this study provides a valuable resource for cereal inflorescence development studies, offering new clues for yield improvement.

## Introduction

Plant meristems harbor a population of pluripotent stem cells and their descendants organized in distinct functional domains with specific functions. In flowering plants, meristems establish inflorescence architecture, and in crop species, contribute to the determination of grain yield (Tanaka et al., 2013). The inflorescence starts when a vegetative shoot apical meristem transitions into the inflorescence meristem (Bergen et al.). In maize, the inflorescence meristem (IM) then proliferates and produces lateral meristems called spikelet pair meristems (SPMs), which develop into spikelet meristems (SMs) then floral meristems (FM) (Irish, 1997). Forward and reverse genetic approaches have identified over 150 genes that regulate inflorescence architecture in maize, such as *KNOTTED1(KN1)* (Jackson et al., 1994), *BARREN STALK1 (BA1)* (Gallavotti et al., 2004), *RAMOSA1 (RA1)* (Vollbrecht et al., 2005), *RAMOSA3 (RA3)* (Satoh-Nagasawa et al., 2006), *BRANCHED SILKLESS1 (BD1)* (Chuck et al., 2002), *ZmACO2* (Ning et al., 2021), and *YIGE1* (Luo et al., 2022) etc. However, genetic pleiotropy and redundancy still limit the insights into inflorescence gene regulatory networks (Lloyd and Meinke, 2012).

Conventional transcriptomics profiles whole plant organs or tissues, and ignores the heterogeneity of cells, making it difficult to address many biological problems (Goldman et al., 2019). With the rapid development of cell capture technology, single-cell transcriptome sequencing (scRNA-seq) has been widely used in plant developmental biology (Zhang et al., 2021a; Zhang et al., 2021b). Such studies provide insights into the roles of cell types in development and their regulatory networks. Single-cell transcriptomes of maize shoot apical meristems, developing ears and roots have produced high-resolution maps of organ development and cell differentiation trajectories (Ortiz-Ramírez et al., 2021; Satterlee et al., 2020; Xu et al., 2021). In these studies, intact tissues were first digested into protoplasts that were subjected to single-cell transcriptome sequencing. However, the original spatial information of cells is lost, resulting in several disadvantages: i) not all cell type can be assigned to spatial locations by marker genes; ii) the same cell type could have different spatial locations and could differentiate into different tissues; iii) the prediction of

developmental trajectories based on single-cell sequencing remains challenging. These challenges are especially apparent in inflorescence primordia, which have sequential development of related meristem types.

Spatial heterogeneity is a key feature of tissue function and cell fate regulation. Therefore, recording transcriptional status with and spatial coordinates is necessary. The DNA nanoball (DNB)-based spatial transcriptome technology (Spatial Enhanced Resolution Omics-sequencing, Stereo-seq), can analyze centimeter-scale samples with subcellular resolution, and can compensate for the shortcomings of single-cell sequencing (Chen et al., 2022). Stereo-seq has been used for *in situ* capture of transcriptomic spatial information in animal models, such as the study of recovery in the salamander telencephalon following injury (Wei et al., 2022) and reconstructing the developmental trajectories of cell-fate transitions and molecular changes during zebrafish embryogenesis (Liu et al., 2022). However, unlike animal cells, most plant cells have a vacuole that occupies most of the cell volume, resulting in ice crystals and fragmentation when tissues are cryo-embedded, significantly limiting the application of spatial transcriptomics. Hence Stereo-seq of plant tissues has been used successfully only in Arabidopsis leaves (Xia et al., 2022).

This study aims to construct a high-resolution spatial transcriptional atlas of developing maize ears by utilizing Stereo-seq. This approach provides a crucial data resource for investigating gene expression, cell type organization, and regulatory networks, ultimately enhancing our understanding of the mechanisms underlying maize ear development and expediting yield improvement efforts.

## Results

### In situ RNA sequencing of developing maize ears by Stereo-seq

The architecture of the maize ear is determined during early development (~ 5–10 mm stage), when meristem initiation, maintenance and determinacy decisions start to form specific organs (Vollbrecht and Schmidt, 2009; Vollbrecht et al., 2005). To generate a spatial transcriptome map of this critical developmental stage, we harvested ~ 6 mm stage ear primordia of the B73 inbred line, containing most meristem types (Fig. 1A). Ears were directly fixed in FAA for 10 minutes and then quick-frozen in optimal cutting temperature (OCT) resin, which can effectively ensure the integrity of the cell and decrease ice crystals that damage the cells (details see Method). Following a Stereo-seq protocol for plant tissues, 10µm thick frozen sections were attached to three 1 cm<sup>2</sup> chips to capture mRNAs. We next used nucleic acid staining of cryosections to highlight the nuclei and check their integrity (Fig. 1B). Intact sections were used to conduct Stereo-seq based on DNA nanoball (DNB) sequencing technology (Chen et al., 2022). The DNB is precast to contain coordinate identities (CID), and unique molecular identifiers (UMI) (Fig. 1B). We ultimately obtained high-quality spatial transcriptomes from four independent developing ear sections, with no transcript signal diffusion according to UMI distribution (Supplemental Fig. 1).

Each DNB spot on the chip is 220 nm in diameter and the center-to-center distance of two adjacent spots is 500 nm. After merging the high-resolution stained images and sequencing data in the Stereomics visualization system (<https://www.stomics.tech/sap/>), we compared the spatial clustering with different

bin sizes, including bin20 (~ 10µm, 20×20 DNB), bin50 (~ 25µm, 50×50 DNB), and bin100 (~ 50µm, 100×100 DNB). We found that using bin50 as bin size produce a better spatial clustering result, with increased cluster numbers and higher accuracy (Supplemental Fig. 2). Therefore, bin50 (~ 25µm) was chosen to represent each spot and construct the spatial transcriptome of developing ears. After filtering low-quality bins (gene number < 150), we totally obtained 34,559 bin50s from four sections, with an average of 8,639 bin50s and 28,530 expressed genes per section (UMI counts greater than 1; Supplemental Table 1). The four sections shared similar gene and UMI numbers in each bin50, supporting the reproducibility of Stereo-seq (Supplemental Fig. 3). In summary, we generated the high-quality *in situ* single-cell RNA sequencing datasets of developing maize ears by using Stereo-seq.

## Spatial clustering and validation of cluster identities

We then pooled bin50s of two adjacent sections, #1 and #2 (from a single ear), for unsupervised clustering analysis after imputation (details see Methods). A uniform manifold approximation and projection (UMAP) plot displayed twelve clusters (Fig. 1C), whose physical distribution on the ear was consistent with the previously published results. More importantly, the clustering of Stereo-seq showed more typical anatomical characteristics in some regions, especially in the inflorescence meristems. (Fig. 1D; Supplemental Figs. 4 and 5).

To verify reliability of Stereo-seq, we next identified the distribution of different cell types in two additional ear sections, #3 and #4. UMAP plots showed that bin50s from the two sections were classified into 11 and 13 clusters, respectively (Supplemental Fig. 6). Using the spatial information of bin50s, we identified the physical location of each cluster (Supplemental Figs. 7 and 8). After comparing the four sections, we found that ten cell types (represented by bin50 clustering) could be repeatedly detected (in at least three sections). Next, we identified a series of cluster-enriched genes and cluster-specific marker genes by analyzing differentially expressed genes among these clusters. More than 70% of marker genes showed the same spatial expression in at least three sections (Supplemental Table 2). To further validate the sensitivity and accuracy of the Stereo-seq, we randomly selected 33 marker genes, identified by using Stereo-seq, and conducted mRNA *in situ* hybridization experiments. This approach could validate the spatial expression patterns of 90% of the genes (30 / 33, Supplemental Data 1). For example, in the Stereo-seq, *kcs15* (*Zm00001eb047970*) and *ZmZNF30* (*Zm00001eb205550*) were observed expressed specifically in meristem epidermis and vasculature respectively, which were confirmed by mRNA *in situ* hybridization (Fig. 1E and 1F). Ultimately, except cortex and pitch, all other common cell types were verified in mRNA *in situ* hybridization. Importantly, we identified and validated four cell/domain types that have not been reported in previous studies (Xu et al., 2021), including those located in critical domain, such as meristem internal (MI), corresponding to the cells of the meristem center, inflorescence meristem tip (IMT), which represents cells in the top ~ 4–5 layers of the inflorescence meristem, and inflorescence meristem cells (IM). These results indicate that Stereo-seq could accurately portray the physical distribution of cell type and unveil specific expression pattern of genes, enabling the discovery of previously unidentified cell types that are not typically detected using traditional scRNA-seq techniques.

## Two major trajectories in developing maize ears

With the precise position of cell types, we constructed a developmental trajectory of the developing ear based on anatomical structure. Our pseudotime analysis using Monocle2 (Qiu et al., 2017), and found seven states in the "branched" trajectory. (Fig. 2A and 2B). Bin50s at state 4, 5 and 6 were mainly located in pitch, cortex and vasculature, while the bin50s at state 1, 2 and 7 were mainly located in inflorescence meristem, inflorescence meristem tip, meristem epidermis and meristem internal (Fig. 2C). We then performed RNA velocity analysis to confirm the trajectory of cell differentiation. Two major trajectories along the pseudotime path were observed (Fig. 2D and Supplemental Fig. 9): (i) bin50s in meristem epidermis were distributed at the early stage of the trajectory, and then transitioned into the meristem base. (ii) bin50s distributed in the upper layer of vasculature differentiated towards the base of the primordia. These results demonstrated at least two developmental trajectories in the maize ear. One is vertical differentiation, and the other is lateral differentiation.

### **Construction of spatial regulatory networks of developing maize ears by integrated analysis of scRNA-seq and Stereo-seq**

Despite the effectiveness of spatial transcriptome in identifying the physical distribution of a cell type, it operates at a non-single-cell level. On the other hand, scRNA-seq enables the capture of more cells and abundant gene expression information, thereby better identifying cell types within tissues. However, the enzymatic hydrolysis of tissues during the process of obtaining cell suspensions leads to the loss of spatial information. Therefore, a combined analysis of scRNA-seq and spatial transcriptome is crucial to improve the resolution of cell types, and unravel their functional characteristics. To explore the spatiotemporal regulatory networks of developing maize ears, we further performed scRNA-seq with ear primordia at the same developmental time point as in the Stereo-seq profiling (at approximately 6-8mm stage). Protoplast suspensions from two independent replicates were made into libraries and sequenced, with comparable UMI and detected genes numbers (see Method, Supplemental Fig. 10, Supplemental Fig. 11A, and Supplemental Table 1). After removing protoplasting-induced genes (Xu et al., 2021) and filtering low-quality cells with more than 5% mitochondrial transcripts or less than 1500 expressed genes, we detected 14,243 cells and 28,627 expressed genes (with count > 1).

Before performing unsupervised analysis, batch effects between the two replicates were removed by the Harmony algorithm (Supplemental Fig. 11B) (Korsunsky et al., 2019). We then visualized clustering using a UMAP plot, where cells were grouped into thirteen clusters (Fig. 3A). To introduce spatial information to the cell clusters of scRNA-seq, we integrated the scRNA-seq and Stereo-seq data by applying STRIDE (Sun et al., 2022) to calculate the proportion of cells (from scRNA-seq) in each spots (bin50s). STRIDE predicted results revealed that cells of single cell cluster (Sc-Cluster) 0, 3, and 4 were distributed on inflorescence meristem, while cells of Sc-Clusters 1, 12 and 11 were mainly on the vasculature, meristem epidermis and meristem internal, respectively (Fig. 3B; Supplemental Fig. 12). The same conclusions could be drawn using bin50s from #3 and #4 sections (Supplemental Figs. 13 and 14). To further verify the accuracy of the integration results, we identified 2,864 genes as cluster-specific markers in scRNA-seq (Supplemental Table 3; min.pct = 0.3, log2fc.threshold = 0.25, padj < 0.01) using the Seurat FindAllMarkers function, and verified their expression pattern in Stereo-seq data (Fig. 3C). With the exception of Sc-Cluster11, at least

five genes provide support for the prediction of the spatial information for each Sc-cluster (Supplemental Fig. 15–17), demonstrating the reliability of STRIDE in integrating scRNA-seq and Stereo-seq data.

To understand gene regulation in developing ears, we next built co-expression networks using scRNAseq datasets through WGCNA (Langfelder and Horvath, 2008). We identified 12 gene modules containing genes that were expressed in a highly coordinated manner (Supplemental Fig. 18A and Supplemental Table 4). For example, 40.2% of genes in module 3 exhibit the highest expression level in vasculature (Sc-Cluster1). Module 3 genes involved in phenylpropanoid metabolic process (GO:0009699; Supplemental Fig. 19A) and phenylpropanoid biosynthesis pathway (KEGG:00940), which serves as the initial step for lignin biosynthesis (Douglas, 1996; Saha et al., 2021). The vasculature, such as xylem tissues comprise several lignified cell types: vessels elements that transport water, and tracheid fibers. Furthermore, 76.9% of genes in module 5 demonstrated the highest expression levels in inflorescence meristem cells (Sc-Cluster4). GO enrichment revealed that module 5 genes were enriched in carbon metabolism pathway, such as organic acid catabolic process activity (GO:0016054; Supplemental Fig. 21B). Moreover, 86.7% of the genes in module7 displayed the highest expression level in meristem epidermis cells (Sc-Cluster12). These genes were significantly enriched in processes related to fatty acid metabolism (GO:0006633) and the biosynthesis of cutin and wax (GO:0010025; Supplemental Fig. 19C). The plant cuticle, composed of a lipophilic layer formed by cutin and cuticular waxes, covers the surface of the epidermis, This layer plays a crucial role in limiting non-stomatal water loss, facilitating gas exchange, and providing mechanical strength and viscoelastic properties (Suh et al., 2005). These results suggest that genes within the same module likely function in same cell types, and are associated with region-specific biological functions of cells.

To explore the core regulatory genes in each of these cell types, gene modules were exported to Cytoscape (Shannon et al., 2003) to construct a co-expression network. The connectivity of each gene was calculated by summing the connection strengths with other genes. Some nodes were considered hub genes, since their expression pattern correlated with numerous genes. The biological function of these hub genes also showed that they likely contributed to the development of the organs in which they were expressed. For example, *OUTER CELL LAYER (OCL)* genes function in cuticle biosynthesis in *Arabidopsis* and maize (Javelle et al., 2010; Luo et al., 2007; Panikashvili et al., 2007). Within module7, we identified *OCL5 (Zm00001eb171720)* as a hub gene with a highest connection to multiple 3-ketoacyl-CoA synthase (*kcs*), and *GLOSSY* genes (Fig. 3D), which are known to participate in wax and cutin biosynthesis (Sturaro et al., 2005; Todd et al., 1999). Furthermore, Stereo-seq data indicated that *OCL5* is specifically expressed in meristem epidermis (Fig. 3G). consistent with the idea that cuticle synthesis process regulated by *OCL*, 3-ketoacyl-CoA synthase, and *GLOSSY* genes occurs in these cells.

We also found multiple *laccase* genes enriched in module3 [*lac9 (Zm00001eb149240)*, *lac7 (Zm00001eb147860)*, *lac14 (Zm00001eb127360)*, *lac11 (Zm00001eb012250)* and *lac2 (Zm00001eb289630)*]. *laccase* genes are implicated in lignin biosynthesis in *Arabidopsis* (Wang et al., 2015; Zhao et al., 2013), suggesting they act similarly to promote vessels development in maize. *peroxidase19 (Zm00001eb131000)* and *peroxidase5 (Zm00001eb282430)* had the highest connectivity to *laccase* genes (Fig. 3E), and Stereo-seq data indicated that *peroxidase19* was specifically expressed in the

vessels (Fig. 3G). Peroxidase enzymes transfer monolignols to lignin, therefore, we assume that *peroxidase* and *laccase* genes can simultaneously regulate lignin composition.

Trehalose-6-phosphate is a key signal in plant development, and over-expression of a trehalose-6-phosphate phosphatase (TPP) in maize ears increased kernel set and harvest index under drought stress (Kataya et al., 2020; Nuccio et al., 2015). Here, we identified module5 as abundant in genes related to trehalose synthesis, including two trehalose-6-phosphate phosphatases (TPP) and five trehalose-6-phosphate synthase (TPS) genes. A NAC transcript factor (*Zm00001eb405590*, also annotated as *nactf25*), served as a hub gene and showed high connection to the TPP and TPS gene cluster (Fig. 3F). Meanwhile, spatial visualization showed that *nactf25* was strongly expressed in the inflorescence meristem (Fig. 3G). Although *nactf25* has not been reported to contribute to maize ear development, NAC-transcription factors directly regulate the expression of TPP genes and influence yield in rice (Li et al., 2022). Therefore, we assume that *nactf25* might affect inflorescence meristem growth by regulating multiple TPP and TPS genes.

To further investigate whether hub genes within the expression network might contribute to maize yield, we estimated narrow-sense heritability ( $h^2$ ) of ear morphology traits related to yield (Yang et al., 2011, Yang et al., 2014). We queried a phenotyped association mapping panel of 507 maize lines (phenotype) for hub genes that highly expressed in vasculature (module3), inflorescence meristem (module5) and meristem epidermis (module7), compared to a distribution of  $h^2$  estimates from random subsets of genes. Using SNPs within 2 kb of genes (Gui et al., 2022), we found that hub genes highly expressed in vasculature (module3) and inflorescence meristem (module5) had greater SNP heritability than the 95th percentile of random genes for cob diameter, kernel row number and ear length. Hub genes highly expressed in meristem epidermis (module7) had greater SNP heritability than the 95th percentile of random genes for kernel number per row (Supplemental Fig. 20, and Supplemental Table 5). In summary, these findings demonstrate the importance of integrating single-cell and spatial transcriptome data, suggesting a novel approach for identifying candidate genes associated with maize yield.

## Two MADS-box gene contribute to stem cell differentiation identified through Stereo-seq dataset

We next ask if the Stereo-seq dataset could facilitate us in understanding how stem cell determinacy shifts from the indeterminate inflorescence meristem to more determinate spikelet and floral meristems. Since these different stem/meristem cells are highly similar, traditional scRNA-seq strategies (Xu et al., 2021) cannot distinguish their spatial positions and expression profiles. Fortunately, our spatial transcriptome map could distinguish various cell types by segmenting their physical location. Therefore, based on their spatial information, we extracted the bin50s in indeterminate and determinate meristems from inflorescence meristem, spikelet meristem and floral meristem. A total of 1,182 bin50s from section #1 [determinate meristem epidermis (ME, n = 837); inflorescence meristem tip (IMT, n = 345)] and 1,394 bin50s from section #2 [ME = 970; IMT = 424] were obtained and re-clustered. This generated three sub-clusters (Fig. 4A and Supplemental Fig. 21A). These sub-clusters were clearly distributed in distinct developing domains, including the indeterminate inflorescence meristem tip (IMT), determinate



spikelet/floral meristem periphery (DMP), and determinate spikelet/floral meristem tip (DMT). These results indicate that our re-clustering could separate highly-similar stem cell type based on their expression profiles, giving an opportunity to investigate changes in gene expression that govern stem cell fate during ear development.

We then conducted a comparative analysis to mine the possible regulators that control stem cell determinacy. A series of differentially expressed genes among the three sub-clusters were detected using the Seurat FindAllMarkers function (Supplemental Table 6; min.pct = 0.3, fold change > 2, padj < 0.01) (Satija et al., 2015). These included two MADS-box genes, *ZmMADS8* and its paralogous *ZmMADS14* (Fig. 4B and Supplemental Fig. 21B), with specific expression in determinate spikelet/floral meristem tips in Stereo-seq, and their expression pattern were validated by mRNA *in situ* hybridization. (Fig. 4C and 4D, Supplemental Fig. 22). A previous study suggested that misexpressing *ZmMADS8* and *DROOPING LEAF2* in the meristem could activate a leaf program, changing meristem identity to make a branch (Du et al., 2022; Kim et al., 2022), implying its function in stem cell determinacy. We therefore generated double knock-out mutants of *ZmMADS8* and *14* by CRISPR/Cas9 genome editing (Supplemental Fig. 23). The single mutants developed normally, producing normal spikelets and fertile florets. In the *CR-Zmmads8/14* double mutants, plant morphology was not significantly different from wild type (Supplemental Fig. 24), the inflorescence and spikelet meristems developed normally. However, the floral meristems were converted to indeterminate ear branches. This indicates that *ZmMADS8* and *14* are key regulators that impose floret identity from stem cells (Fig. 4E-4P). In summary, our results indicate that *ZmMADS8* and *ZmMADS14* redundantly play a critical function in programming the differentiation of pluripotent stem cells into determinate floral meristems during maize ear development. The spatial transcriptome generated by Stereo-seq provided new insights into crop inflorescence development and facilitated the identification of key regulators underlying fine developing processes.

## Discussion

The maize ear is an excellent model for study of development biology and optimizing morphology to achieve high grain yield (Li et al., 2018; Liu et al., 2021; Wu et al., 2018). Many spatiotemporally expressed genes acting early in development determine the size and kernel number of maize ears, requiring us to understand gene expression at the spatial and single-cell levels. A previous study generated a single-cell resolution map of maize developing ear primordia by scRNA-seq from protoplasts, and showed that scRNA-seq data could facilitate genetic studies (Xu et al., 2021). However, limited by the number of marker genes, the molecular definition and spatial information of cell types are largely incomplete and difficult to identify in plant. The recently developed DNA nanoball-based spatial transcriptome technology, Stereo-seq, has been applied in animal models (Chen et al., 2022; Liu et al., 2022; Wei et al., 2022) and *Arabidopsis* leaves (Xia et al., 2022), it also allowed us to generate a precise spatial transcriptome profile and to clearly distinguish twelve cell types (#1 and #2 sections). Ultimately, Eight of the twelve cell types were consistent with previously scRNA-seq study, and four newly defined cell types were also supported by mRNA *in situ* hybridization evidence, including inflorescence meristem, inflorescence meristem periphery, inflorescence

meristem tip and meristem internal. These novel findings will substantially enhance our understanding of maize developing ear cell types and their respective biological function.

By employing a deconvolution algorithm to evaluate the similarity between scRNA-seq and spatial transcriptome data, we inferred the identities of six clusters and validated three spatially resolved gene modules in scRNA-seq. Furthermore, we found that the hub genes and the core co-expression networks were closely related to the biological function of their cell types/tissue. Modifying such hub genes could offer a new solution to avoid gene redundancy in breeding strategies. For example, the hub gene *nactf25* was co-expressed with a TPP and TPS gene cluster, which affect the synthesis of trehalose-6-phosphate and regulate maize ear development (Claeys et al., 2019). *nactf25* may be used to overcome the redundancy of the TPP gene in future breeding strategies, which needs further verification. These results suggest that Stereo-seq has a significant advantage for constructing a comprehensive and precise spatial transcriptome map of maize ear. In addition, it can also be successfully used to infer the cell type identity of scRNA-seq. In the near future, as Stereo-seq continues to evolve and enhance its capacity for *in situ* mRNA capture, the integration of spatial transcriptome and single cell transcriptome will also be more precise and efficient.

Based on our high-resolution Stereo-seq data, we find two major trajectories initiated from meristem cells. A related major question in maize biology is how the IM differentiates into SM and FM. Due to their similarity, these meristems cell could not be resolved in scRNAseq analysis (Xu et al., 2021). Taking advantage of our spatial transcriptome, we extracted and re-clustered indeterminate and determinate meristem components from IM, SM and FM, and found two genes, *ZmMADS8* and *ZmMADS14*, expressed specifically in the determinate spikelet/floral meristem tips, and control floral stem cell determinacy. Therefore, the Stereo-seq spatial transcriptome provides new insights into maize inflorescence development and facilitated the identification of key regulators underlying specific developmental processes that could inform crop yield improvement.

In summary, the implementation of Stereo-seq technology in our study has proven to be a powerful tool for obtaining a comprehensive spatial transcriptome map of the maize ear. The data generated through this approach not only serves as a valuable genetic resource, but also provides detailed insights into the development of the maize ear at a higher resolution. The knowledge gained here can be used to inform the maize yield improvement process, and deep our understanding of inflorescence meristem development. Additionally, our exploration of the application of Stereo-seq methodology in this context contributes valuable experience to the field of plant spatial transcriptomics, paving the way for future advancements in this area.

## Declarations

### ACKNOWLEDGEMENTS

This research was supported by funding from the National Key Research and Development Program of China (2022YFD1201500, 2020YFE0202300) to J.Y., the National Natural Science Foundation of China

(32222062) to N.Y., and NSF-IOS 1934388 to D.J. Computation resources were provided by the high-throughput computing platform of the National Key Laboratory of Crop Genetic Improvement at Huazhong Agricultural University and supported by H. Liu.

### **Data availability**

scRNA-seq and Stereo-seq data from this study can be found in CNGBdb (<https://db.cngb.org/>), and under project accession code CNP0004249.

## **Method and materials**

### **Plant growth conditions and tissue fixation**

Maize B73 inbred plants were grown in the field (April - July) at Huazhong Agricultural University in Wuhan, Hubei, or in a greenhouse with 12 hours of daylight, at temperatures ranging from 26–28°C during the day and 22–24°C at night. Developing ears (~ 6mm) were collected at eleven or twelve leaf stages and immediately fixed in a 50% formalin-acetic acid-alcohol (FAA) solution (50% absolute ethanol, 10% formaldehyde, 5%acetic acid, v/v/v ) for 10 minutes. The tissues were then treated with 2% sucrose solution (50% 1 × PBS buffer, pH = 7.4, 2% sugar, v/m) and evacuated twice on ice for 15 minutes each, with the liquid being changed once in the middle. The tissues were then embedded in pre-chilled OCT (Sakura), snap-frozen in liquid nitrogen pre-chilled isopentane for 10 seconds, and stored at -80°C until processed.

The maize double mutant *CR-Zmmads8/14* transgenic lines were generated in the KN5855 genetic background. The mutant sites were detected by PCR with primers (list in Supplemental Table 7). The *CR-Zmmads8/14* double mutant was crossed with wild-type and then self-crossed to segregate the *CR-Zmmads8* and *CR-Zmmads14* single mutants, which were evaluated in the field in two environments: summer 2020 in Wuhan (30°N, 114°E) and spring 2021 in Sanya (18.34°N, 109.62°E), China. The SEM observations of ears were conducted at the 7–8 leaf stage.

### **SEM Observation**

Immature ears (~ 5–6 mm) of B73, KN5855, *CR-Zmmads8*, *CR-Zmmads14*, and *CR-Zmmads8/14* were collected from plants grown in the field at Huazhong Agricultural University in Wuhan, Hubei, or in a greenhouse maintained at 26–28°C during the day and 22–24°C at night with a 12-hour light-dark cycle. The ears quickly removed the bracts and then observed using a Jeol JSM-7900F SEM, as previously described (Chuck et al., 2010).

### **In situ hybridization**

Immature maize B73 ears, measuring 5–6 mm in length, were fixed in a 4% PFA solution (4g of paraformaldehyde (Sigma-Aldrich) dissolved in 100 mL of 1× PBS, pH 6.5–7). The ears were dehydrated using a series of ethanol concentrations (30%, 50% and 70%) and embedded in paraplast plus (Sigma P3683) and sectioned to a thickness of 8µm. To generate sense and antisense RNA probes, probe fragments were amplified by PCR using primers listed in Supplemental Table 7. A sequence

(CATTAAACGACTCACTATAGGG) was incorporated in the 5' and 3' primers for sense and antisense RNA probes. The probes were then transcribed in vitro using T7 RNA polymerase (Roche) and labeled with digoxigenin-UTP (Roche). Finally, RNA hybridization, immunologic detection, and signal capture of the hybridized probes were performed as previously described (Jackson et al., 1994).

### **Stereo-seq library preparation and sequencing**

The experimental method is based on the previously reported Stereo-seq standard protocol V1.1 with some modifications (Chen et al., 2022). The embedded developing ear tissues were longitudinally sectioned at 10  $\mu$ m thickness (Leica, CM1950). Tissue sections were adhered to the Stereo-seq chip surface and incubated at 37°C for 2 minutes. Tissues were fixed in methanol and incubated at -20°C for 40 minutes, followed by nucleic acid dye staining (Thermo fisher, Q10212) for 5 mins. The same sections were also used for bright-field imaging, both images were taken with Motic PA53 Scanner. Tissue sections were de-crosslinked in TE buffer (10  $\mu$ M Tris, 1  $\mu$ M EDTA, PH = 8) at 55°C for 1 hour. Tissue sections were permeabilized at 37°C for 12 minutes, and incubated overnight at 42°C for reverse transcription and cDNA synthesis. Afterward, tissue was digested at 37°C for 30 minutes, and treated with Exonuclease I (NEB, M0293L) for 1 hour at 37°C. The cDNA products were purified using the Ampure XP Beads (Vazyme, N411-03) (0.6x and 0.15x), used for DNB generation and finally sequenced (paired-end 50 bp or paired-end 100 bp) on a MGI DNBSEQ-Tx sequencer.

### **Raw Stereo-seq data processing and quality control**

Stereo-seq raw reads were generated from a MGI DNBSEQ-T5 sequencer. Read 1 contained CID and UMI sequences (CID: 1-25bp, UMI: 26-35bp), while read 2 contained the cDNA sequence. Retained reads were then aligned to the reference genome B73 (Hufford et al., 2021) via STAR (Dobin et al., 2013). and mapped reads with MAPQ 10 were counted and annotated to their corresponding genes using an in-house script (available at <https://github.com/BGIResearch/handleBam>) and generated a gene-location expression matrix containing location information.

### **Binning data of spatial Stereo-seq**

After obtaining raw spatial data, transcripts captured by 50x50 DNBs were merged into one bin50. We treated the bin50 as the fundamental analysis unit, and bin IDs were composed of X and Y coordinates on the capture chip. The threshold for filtering low-quality bins was set to no more than 150 or higher than 5000 gene counts. After filtering, the remaining bin50s (details can be found in Supplementary Table 1) were included in the downstream analysis.

### **Recovering missing value and Unsupervised clustering of Stereo-seq data**

We performed normalization in the origin dataset (LogNormalize, scaling factor 10,000) using the R package Seurat (4.1.1) (Satija et al., 2015). We scaled the data using the ScaleData function and identified 2,000 highly variable features using the FindNeighbors function. Finally, we used the FindClusters function to identify all cell clusters. However, many genes were only expressed in a subset of bin50s. We therefore used the Seurat Wrapper function RunALRA (Butler et al., 2018; Stuart et al., 2019) to impute missing

expression values, increasing the non-zero ratio of expressed genes from 3.0–66.4% in #1 and #2 sections, from 3.8–62.9% in section #3 and from 3.1–72.6% in section #4 (Supplemental Fig. 25). The physical distribution of cell types before and after imputation is consistent (Supplemental Fig. 26). More importantly, the clustering of imputed datasets showed more typical anatomical characteristics in some regions, especially in the meristems and vasculature (Fig. 1D; Supplemental Figs. 4 and 5).

### **Identifying marker genes of clusters in Stereo-seq and scRNA-seq data**

The cluster-enriched genes were computed with FindMarkers function of Seurat R package (Satija et al., 2015), with parameter “log2fc.threshold = 0.25, p\_val\_adj < 0.01”. The following threshold were applied to identify cluster-specific marker genes: the log2 fold change of genes was > 0.25 and the proportion of marker genes expressed in cells among corresponding clusters was > 30%.

### **Monocle 2 analysis**

The pseudotime trajectories were reconstructed using Monocle2 (2.22.0) (Qiu et al., 2017). The count matrix was first converted to a CellDataSet object. Then, differentially expressed genes were identified using the FindAllMarkers function in the Seurat R package (min.pct = 0.5, log2fc.threshold = 1), and filtered by p\_val\_adj < 0.01. Dimensional reduction clustering and pseudotime trajectory inference were performed using the reduceDimension function and the orderCells function with default parameters, respectively.

### **RNA velocity analysis**

We divided the gene status into three types - unspliced, spliced, and ambiguous - using the CIGAR alignment information in the BAM file, as previously described (La Manno et al., 2018). To further preprocess the data, we scaled the spatial position of the sections on the chips and removed invalid reads and alignment results located on the section's periphery. The preprocessed BAM file was then used to generate a sparse matrix, which was subsequently converted to an adata format using the R package anndata (Wolf et al., 2018) (<https://github.com/theislab/anndata>). The entire process can also be performed using a local script (<https://github.com/wjwei-handsome/bam2adata>).

We performed data normalization and clustering using default parameters in scanpy (Wolf et al., 2018) and scvelo (Bergen et al., 2020) packages. High variable genes were selected as feature genes, and dimension reduction was performed via UMAP. Subsequently, kinetic parameters and gene-wise RNA velocity vectors were estimated on the normalized matrix and projected onto the visualized spatial plot to retain spatial information. We used streamlines to visualize the velocity vector flows on the maize 6mm ear section.

### **Protoplast preparation**

Protoplast preparation was conducted as previously described (Tu et al., 2020; Yoo et al., 2007). In brief, approximately 30 6 mm developing ears were dissected with sharp razors into 0.5-1 mm slices in 0.4 M mannitol. After discarding the mannitol, the slices were immediately transferred into a 35-mm Petri dish containing 4 ml of enzyme solution, consisting of 0.6 M D-mannitol, 1% (w/v) Cellulase Onozuka R-10 (Research Products International [RPI]), 0.2% (w/v) Macerozyme R-10 (RPI), 20 mM 2-(N-Morpholino)

ethanesulfonic acid (MES)(pH = 5.7), 1 mM MgCl<sub>2</sub>, 1 mM CaCl<sub>2</sub>, 1 mM 2-mercaptoethanol, and 0.1% (w/v) bovine serum albumin (BSA) (Sigma-Aldrich).

(Notes: Before the addition of CaCl<sub>2</sub>, 2-mercaptoethanol and BSA, the solution was heated to 55°C for 10 minutes to inactivate proteases and facilitate enzyme solubility. Once the solution cooled to room temperature, CaCl<sub>2</sub>, 2-mercaptoethanol and BSA were added. Finally, sterile Milli-Q water was added to reach a final volume of 4 ml. The resulting enzyme solution was filtered through a 0.45 µm syringe filter into a 35-mm Petri dish).

Tissues were kept under vacuum (30 kPa) for 30 min in the dark at room temperature. Tissue digestion was carried out with gentle shaking (40 rpm on a platform shaker) in the dark at 28°C for 2 hours. Following digestion, an equal volume of W5 solution (2 mM MES adjusted to pH 5.7 with KOH, 154 mM NaCl, 125 mM CaCl<sub>2</sub>, and 5 mM KCl) was added. The mixture was gently pipetted several times with a Pasteur pipette. Protoplasts that passed through a 40 µm cell strainer (Falcon) and a 30 µm cell strainer (pluriStrainer) were filtered into a 14 ml round-bottom Falcon tube (Falcon), and collected by centrifugation at 100 × g for 6 minutes at 4°C with slow acceleration/braking. The supernatant was gently removed without disturbing the pellet, then resuspended gently with 6 ml of cold W5 solution and washed twice using the same centrifugation conditions. The cells were resuspended in 3 ml of cold W5 solution. The tube was placed on ice for 30 minutes to facilitate the sedimentation of intact cells. The supernatant containing dead cells or debris was removed as much as possible using a Pasteur pipette. The pellet was resuspended with 500 µl of cold W5 solution and transferred to a 2 ml microcentrifuge tube. The protoplasts were stained with 10 µg/mL of fluorescein diacetate (FDA) to check cell concentration and viability with a hemocytometer under a fluorescent microscope. More than 20,000 high quality protoplasts with viability ≥ 80% were immediately loaded onto the SCOPE-chip (Singleron) to collect single cells. Library preparation was followed the manufactures instructions of the GEXSCOPE single cell RNA library kits (Singleron).

### **Single cell RNA-seq analysis**

The sequencing reads from two biological replicates of 6mm B73 ear were aligned to the maize v5 reference genome using the CeleScope bioinformatics analysis pipeline (version 1.6.1) available at <https://github.com/singleron-RD/CeleScope>. Probable doublets were removed using DoubletFinder (McGinnis et al., 2019). After obtaining the single-cell raw expression matrix, we filtered out low-quality cells based on the number of genes detected (< 1500 or > 10000), excluded cells with a high percentage of mitochondrial genes (> 5%) to avoid cytoplasmic RNA leakage. Additionally, we excluded protoplasting-responsive genes identified in a previous study (Xu et al., 2021) to avoid potential confounding effects. Finally, we retained 19,584 single cells and 28,587 genes for downstream analysis.

Downstream analyses were mainly performed using the Seurat package (version 4.1.1) (Satija et al., 2015). Normalized data were generated using the NormalizeData function (LogNormalize, scaling factor 10,000) and variable genes were detected using the FindVariableGenes function (vst method, 2000 features). The scaled data were then subjected to PCA analysis using the RunPCA function. In order to integrate multiple

samples, we used the RunHarmony function to correct batch effects. Subsequently, a SNN graph was constructed, and cells were clustered based on Louvain (using the FindNeighbors and FindClusters functions). Finally, the data was visualized using non-linear dimensional reduction algorithms (using the RunUMAP function).

### **Integrating scRNA-seq and Stereo-seq data.**

The proportion of cells from different Sc-clusters in the spots were estimated using the STRIDE deconvolve function (Sun et al., 2022). The proportion of cells from different Sc-clusters in the bin50s of section #1 and #2 were list in Supplemental Table 8, the proportion of cells from different Sc-clusters in the bin50s of section #3 were list in Supplemental Table 9, the proportion of cells from different Sc-clusters in the bin50s of section #4 were list in Supplemental Table 10.

### **Constructing co-expression network, GO and KEGG enrichment analysis**

The gene co-expression network was constructed using the WGCNA package (version 1.71) (Langfelder and Horvath, 2008). We calculated the average expression level of genes in each scRNA-seq cluster and used it as the input file of WGCNA. After obtaining the gene modules and weight of connection degrees between each gene based on their expression patterns, we performed gene set enrichment analysis using the gprofiler web tool (<https://biit.cs.ut.ee/gprofiler/gost>). The network diagram was generated using Cytoscape (version 3.7.1) (Shannon et al., 2003).

### **SNP Heritability analysis**

We used the LDAK software v5.2 (Speed et al., 2012) to estimate narrow-sense heritability ( $h^2$ ) from subsets of hub gene SNPs located 2 kb upstream and downstream. To test if the heritability for a given trait was greater than expected by chance, we estimated the heritability for 1000 permutations using a random subset of maize genes. For each permutation, genes with at least one SNP within the genic region were randomly selected to create a subset with a size within  $\pm 5$  of the target set. A target set was considered significant for a given trait if its heritability exceeded the top 5% of permuted values.

## **References**

1. Bergen, V., Lange, M., Peidli, S., Wolf, F.A., and Theis, F.J. (2020). Generalizing RNA velocity to transient cell states through dynamical modeling. *Nat Biotechnol.* 38: 1408-1414.
2. Butler, A., Hoffman, P., Smibert, P., Papalexi, E., and Satija, R. (2018). Integrating single-cell transcriptomic data across different conditions, technologies, and species. *Nat Biotechnol.* 36: 411-420.
3. Chen, A., Liao, S., Cheng, M., Ma, K., Wu, L., Lai, Y., Qiu, X., Yang, J., Xu, J., Hao, S., et al. (2022). Spatiotemporal transcriptomic atlas of mouse organogenesis using DNA nanoball-patterned arrays. *Cell.* 185: 1777-1792.e1721.

4. Chuck, G., Muszynski, M., Kellogg, E., Hake, S., and Schmidt, R.J. (2002). The control of spikelet meristem identity by the branched silkless1 gene in maize. *Science*. 298: 1238-1241.
5. Chuck, G., Whipple, C., Jackson, D., and Hake, S. (2010). The maize SBP-box transcription factor encoded by tasselsheath4 regulates bract development and the establishment of meristem boundaries. *Development*. 137: 1243-1250.
6. Claeys, H., Vi, S.L., Xu, X., Satoh-Nagasawa, N., Eveland, A.L., Goldshmidt, A., Feil, R., Beggs, G.A., Sakai, H., Brennan, R.G., et al. (2019). Control of meristem determinacy by trehalose 6-phosphate phosphatases is uncoupled from enzymatic activity. *Nat Plants*. 5: 352-357.
7. Dobin, A., Davis, C.A., Schlesinger, F., Drenkow, J., Zaleski, C., Jha, S., Batut, P., Chaisson, M., and Gingeras, T.R. (2013). STAR: ultrafast universal RNA-seq aligner. *Bioinformatics*. 29: 15-21.
8. Douglas, C.J. (1996). Phenylpropanoid metabolism and lignin biosynthesis: from weeds to trees. *Trends in Plant Science*. 1: 171-178.
9. Du, Y., Wu, B., Xing, Y., and Zhang, Z. (2022). Conservation and divergence: Regulatory networks underlying reproductive branching in rice and maize. *J Adv Res*. 41: 179-190.
10. Gallavotti, A., Zhao, Q., Kyojuka, J., Meeley, R.B., Ritter, M.K., Doebley, J.F., Pè, M.E., and Schmidt, R.J. (2004). The role of barren stalk1 in the architecture of maize. *Nature*. 432: 630-635.
11. Goldman, S.L., MacKay, M., Afshinnekoo, E., Melnick, A.M., Wu, S., and Mason, C.E. (2019). The Impact of Heterogeneity on Single-Cell Sequencing. *Front Genet*. 10: 8.
12. Gui, S., Wei, W., Jiang, C., Luo, J., Chen, L., Wu, S., Li, W., Wang, Y., Li, S., Yang, N., et al. (2022). A pan-Zea genome map for enhancing maize improvement. *Genome Biol*. 23: 178.
13. Hufford, M.B., Seetharam, A.S., Woodhouse, M.R., Chougule, K.M., Ou, S., Liu, J., Ricci, W.A., Guo, T., Olson, A., Qiu, Y., et al. (2021). De novo assembly, annotation, and comparative analysis of 26 diverse maize genomes. *Science*. 373: 655-662.
14. Irish, E. (1997). Class II tassel seed mutations provide evidence for multiple types of inflorescence meristems in maize (Poaceae). *Am J Bot*. 84: 1502.
15. Jackson, D., Veit, B., and Hake, S. (1994). Expression of maize KNOTTED1 related homeobox genes in the shoot apical meristem predicts patterns of morphogenesis in the vegetative shoot. *Development*. 120: 405-413.
16. Javelle, M., Vernoud, V., Depège-Fargeix, N., Arnould, C., Oursel, D., Domergue, F., Sarda, X., and Rogowsky, P.M. (2010). Overexpression of the epidermis-specific homeodomain-leucine zipper IV transcription factor Outer Cell Layer1 in maize identifies target genes involved in lipid metabolism and cuticle biosynthesis. *Plant Physiol*. 154: 273-286.
17. Kataya, A.R.A., Elshobaky, A., Heidari, B., Dugassa, N.F., Thelen, J.J., and Lillo, C. (2020). Multi-targeted trehalose-6-phosphate phosphatase I harbors a novel peroxisomal targeting signal 1 and is essential for flowering and development. *Planta*. 251: 98.
18. Kim, D.E., Jeong, J.-h., Kang, Y.M., Park, Y.-H., Lee, Y.-J., Kang, J.-s., Choi, Y.-W., Son, B.-G., Kim, S.T., Jackson, D., et al. (2022). The Impact of Fasciation on Maize Inflorescence Architecture. *Journal of Plant Biology*. 65: 87-98.



19. Korsunsky, I., Millard, N., Fan, J., Slowikowski, K., Zhang, F., Wei, K., Baglaenko, Y., Brenner, M., Loh, P.R., and Raychaudhuri, S. (2019). Fast, sensitive and accurate integration of single-cell data with Harmony. *Nat Methods*. 16: 1289-1296.
20. La Manno, G., Soldatov, R., Zeisel, A., Braun, E., Hochgerner, H., Petukhov, V., Lidschreiber, K., Kastrioti, M.E., Lönnerberg, P., Furlan, A., et al. (2018). RNA velocity of single cells. *Nature*. 560: 494-498.
21. Langfelder, P., and Horvath, S. (2008). WGCNA: an R package for weighted correlation network analysis. *BMC Bioinformatics*. 9: 559.
22. Li, M., Zhong, W., Yang, F., and Zhang, Z. (2018). Genetic and Molecular Mechanisms of Quantitative Trait Loci Controlling Maize Inflorescence Architecture. *Plant Cell Physiol*. 59: 448-457.
23. Li, Z., Wei, X., Tong, X., Zhao, J., Liu, X., Wang, H., Tang, L., Shu, Y., Li, G., Wang, Y., et al. (2022). The OsNAC23-Tre6P-SnRK1a feed-forward loop regulates sugar homeostasis and grain yield in rice. *Mol Plant*. 15: 706-722.
24. Liu, C., Li, R., Li, Y., Lin, X., Zhao, K., Liu, Q., Wang, S., Yang, X., Shi, X., Ma, Y., et al. (2022). Spatiotemporal mapping of gene expression landscapes and developmental trajectories during zebrafish embryogenesis. *Dev Cell*. 57: 1284-1298.e1285.
25. Liu, L., Gallagher, J., Arevalo, E.D., Chen, R., Skopelitis, T., Wu, Q., Bartlett, M., and Jackson, D. (2021). Enhancing grain-yield-related traits by CRISPR-Cas9 promoter editing of maize CLE genes. *Nat Plants*. 7: 287-294.
26. Lloyd, J., and Meinke, D. (2012). A comprehensive dataset of genes with a loss-of-function mutant phenotype in Arabidopsis. *Plant Physiol*. 158: 1115-1129.
27. Luo, B., Xue, X.Y., Hu, W.L., Wang, L.J., and Chen, X.Y. (2007). An ABC transporter gene of Arabidopsis thaliana, AtWBC11, is involved in cuticle development and prevention of organ fusion. *Plant Cell Physiol*. 48: 1790-1802.
28. Luo, Y., Zhang, M., Liu, Y., Liu, J., Li, W., Chen, G., Peng, Y., Jin, M., Wei, W., Jian, L., et al. (2022). Genetic variation in YIGE1 contributes to ear length and grain yield in maize. *New Phytol*. 234: 513-526.
29. McGinnis, C.S., Murrow, L.M., and Gartner, Z.J. (2019). DoubletFinder: Doublet Detection in Single-Cell RNA Sequencing Data Using Artificial Nearest Neighbors. *Cell Syst*. 8: 329-337.e324.
30. Ning, Q., Jian, Y., Du, Y., Li, Y., Shen, X., Jia, H., Zhao, R., Zhan, J., Yang, F., Jackson, D., et al. (2021). An ethylene biosynthesis enzyme controls quantitative variation in maize ear length and kernel yield. *Nat Commun*. 12: 5832.
31. Nuccio, M.L., Wu, J., Mowers, R., Zhou, H.P., Meghji, M., Primavesi, L.F., Paul, M.J., Chen, X., Gao, Y., Haque, E., et al. (2015). Expression of trehalose-6-phosphate phosphatase in maize ears improves yield in well-watered and drought conditions. *Nat Biotechnol*. 33: 862-869.
32. Ortiz-Ramírez, C., Guillotin, B., Xu, X., Rahni, R., Zhang, S., Yan, Z., Coqueiro Dias Araujo, P., Demesa-Arevalo, E., Lee, L., Van Eck, J., et al. (2021). Ground tissue circuitry regulates organ complexity in maize and Setaria. *Science*. 374: 1247-1252.
33. Panikashvili, D., Savaldi-Goldstein, S., Mandel, T., Yifhar, T., Franke, R.B., Höfer, R., Schreiber, L., Chory, J., and Aharoni, A. (2007). The Arabidopsis DESPERADO/AtWBC11 transporter is required for cutin and wax secretion. *Plant Physiol*. 145: 1345-1360.

34. Qiu, X., Mao, Q., Tang, Y., Wang, L., Chawla, R., Pliner, H.A., and Trapnell, C. (2017). Reversed graph embedding resolves complex single-cell trajectories. *Nat Methods*. 14: 979-982.
35. Saha, P., Lin, F., Thibivilliers, S., Xiong, Y., Pan, C., and Bartley, L.E. (2021). Phenylpropanoid Biosynthesis Gene Expression Precedes Lignin Accumulation During Shoot Development in Lowland and Upland Switchgrass Genotypes. *Front Plant Sci*. 12: 640930.
36. Satija, R., Farrell, J.A., Gennert, D., Schier, A.F., and Regev, A. (2015). Spatial reconstruction of single-cell gene expression data. *Nat Biotechnol*. 33: 495-502.
37. Satoh-Nagasawa, N., Nagasawa, N., Malcomber, S., Sakai, H., and Jackson, D. (2006). A trehalose metabolic enzyme controls inflorescence architecture in maize. *Nature*. 441: 227-230.
38. Satterlee, J.W., Strable, J., and Scanlon, M.J. (2020). Plant stem-cell organization and differentiation at single-cell resolution. *Proc Natl Acad Sci U S A*. 117: 33689-33699.
39. Shannon, P., Markiel, A., Ozier, O., Baliga, N.S., Wang, J.T., Ramage, D., Amin, N., Schwikowski, B., and Ideker, T. (2003). Cytoscape: a software environment for integrated models of biomolecular interaction networks. *Genome Res*. 13: 2498-2504.
40. Speed, D., Hemani, G., Johnson, M.R., and Balding, D.J. (2012). Improved heritability estimation from genome-wide SNPs. *Am J Hum Genet*. 91: 1011-1021.
41. Stuart, T., Butler, A., Hoffman, P., Hafemeister, C., Papalexi, E., Mauck, W.M., 3rd, Hao, Y., Stoeckius, M., Smibert, P., and Satija, R. (2019). Comprehensive Integration of Single-Cell Data. *Cell*. 177: 1888-1902.e1821.
42. Sturaro, M., Hartings, H., Schmelzer, E., Velasco, R., Salamini, F., and Motto, M. (2005). Cloning and characterization of GLOSSY1, a maize gene involved in cuticle membrane and wax production. *Plant Physiol*. 138: 478-489.
43. Suh, M.C., Samuels, A.L., Jetter, R., Kunst, L., Pollard, M., Ohlrogge, J., and Beisson, F. (2005). Cuticular lipid composition, surface structure, and gene expression in Arabidopsis stem epidermis. *Plant Physiol*. 139: 1649-1665.
44. Sun, D., Liu, Z., Li, T., Wu, Q., and Wang, C. (2022). STRIDE: accurately decomposing and integrating spatial transcriptomics using single-cell RNA sequencing. *Nucleic Acids Res*. 50: e42.
45. Tanaka, W., Pautler, M., Jackson, D., and Hirano, H.Y. (2013). Grass meristems II: inflorescence architecture, flower development and meristem fate. *Plant Cell Physiol*. 54: 313-324.
46. Todd, J., Post-Beittenmiller, D., and Jaworski, J.G. (1999). KCS1 encodes a fatty acid elongase 3-ketoacyl-CoA synthase affecting wax biosynthesis in Arabidopsis thaliana. *Plant J*. 17: 119-130.
47. Tu, X., Mejía-Guerra, M.K., Valdes Franco, J.A., Tzeng, D., Chu, P.Y., Shen, W., Wei, Y., Dai, X., Li, P., Buckler, E.S., et al. (2020). Reconstructing the maize leaf regulatory network using ChIP-seq data of 104 transcription factors. *Nat Commun*. 11: 5089.
48. Vollbrecht, E., Springer, P.S., Goh, L., Buckler, E.S., and Martienssen, R. (2005). Architecture of floral branch systems in maize and related grasses. *Nature*. 436: 1119-1126.
49. Wang, J., Feng, J., Jia, W., Chang, S., Li, S., and Li, Y. (2015). Lignin engineering through laccase modification: a promising field for energy plant improvement. *Biotechnol Biofuels*. 8: 145.

50. Wei, X., Fu, S., Li, H., Liu, Y., Wang, S., Feng, W., Yang, Y., Liu, X., Zeng, Y.Y., Cheng, M., et al. (2022). Single-cell Stereo-seq reveals induced progenitor cells involved in axolotl brain regeneration. *Science*. 377: eabp9444.
51. Wolf, F.A., Angerer, P., and Theis, F.J. (2018). SCANPY: large-scale single-cell gene expression data analysis. *Genome Biol.* 19: 15.
52. Wu, Q., Xu, F., and Jackson, D. (2018). All together now, a magical mystery tour of the maize shoot meristem. *Curr Opin Plant Biol.* 45: 26-35.
53. Xia, K., Sun, H.X., Li, J., Li, J., Zhao, Y., Chen, L., Qin, C., Chen, R., Chen, Z., Liu, G., et al. (2022). The single-cell stereo-seq reveals region-specific cell subtypes and transcriptome profiling in Arabidopsis leaves. *Dev Cell.* 57: 1299-1310.e1294.
54. Xu, X., Crow, M., Rice, B.R., Li, F., Harris, B., Liu, L., Demesa-Arevalo, E., Lu, Z., Wang, L., Fox, N., et al. (2021). Single-cell RNA sequencing of developing maize ears facilitates functional analysis and trait candidate gene discovery. *Dev Cell.* 56: 557-568.e556.
55. Yang, N., Lu, Y., Yang, X., Huang, J., Zhou, Y., Ali, F., Wen, W., Liu, J., Li, J., and Yan, J. (2014). Genome wide association studies using a new nonparametric model reveal the genetic architecture of 17 agronomic traits in an enlarged maize association panel. *PLoS Genet.* 10: e1004573.
56. Yang, X., Gao, S., Xu, S., Zhang, Z., Prasanna, B.M., Li, L., Li, J., and Yan, J.J.M.B. (2011). Characterization of a global germplasm collection and its potential utilization for analysis of complex quantitative traits in maize. 28: 511-526.
57. Yoo, S.D., Cho, Y.H., and Sheen, J. (2007). Arabidopsis mesophyll protoplasts: a versatile cell system for transient gene expression analysis. *Nat Protoc.* 2: 1565-1572.
58. Zhang, T.Q., Chen, Y., Liu, Y., Lin, W.H., and Wang, J.W. (2021a). Single-cell transcriptome atlas and chromatin accessibility landscape reveal differentiation trajectories in the rice root. *Nat Commun.* 12: 2053.
59. Zhang, T.Q., Chen, Y., and Wang, J.W. (2021b). A single-cell analysis of the Arabidopsis vegetative shoot apex. *Dev Cell.* 56: 1056-1074.e1058.
60. Zhao, Q., Nakashima, J., Chen, F., Yin, Y., Fu, C., Yun, J., Shao, H., Wang, X., Wang, Z.Y., and Dixon, R.A. (2013). Laccase is necessary and nonredundant with peroxidase for lignin polymerization during vascular development in Arabidopsis. *Plant Cell.* 25: 3976-3987.

## Figures

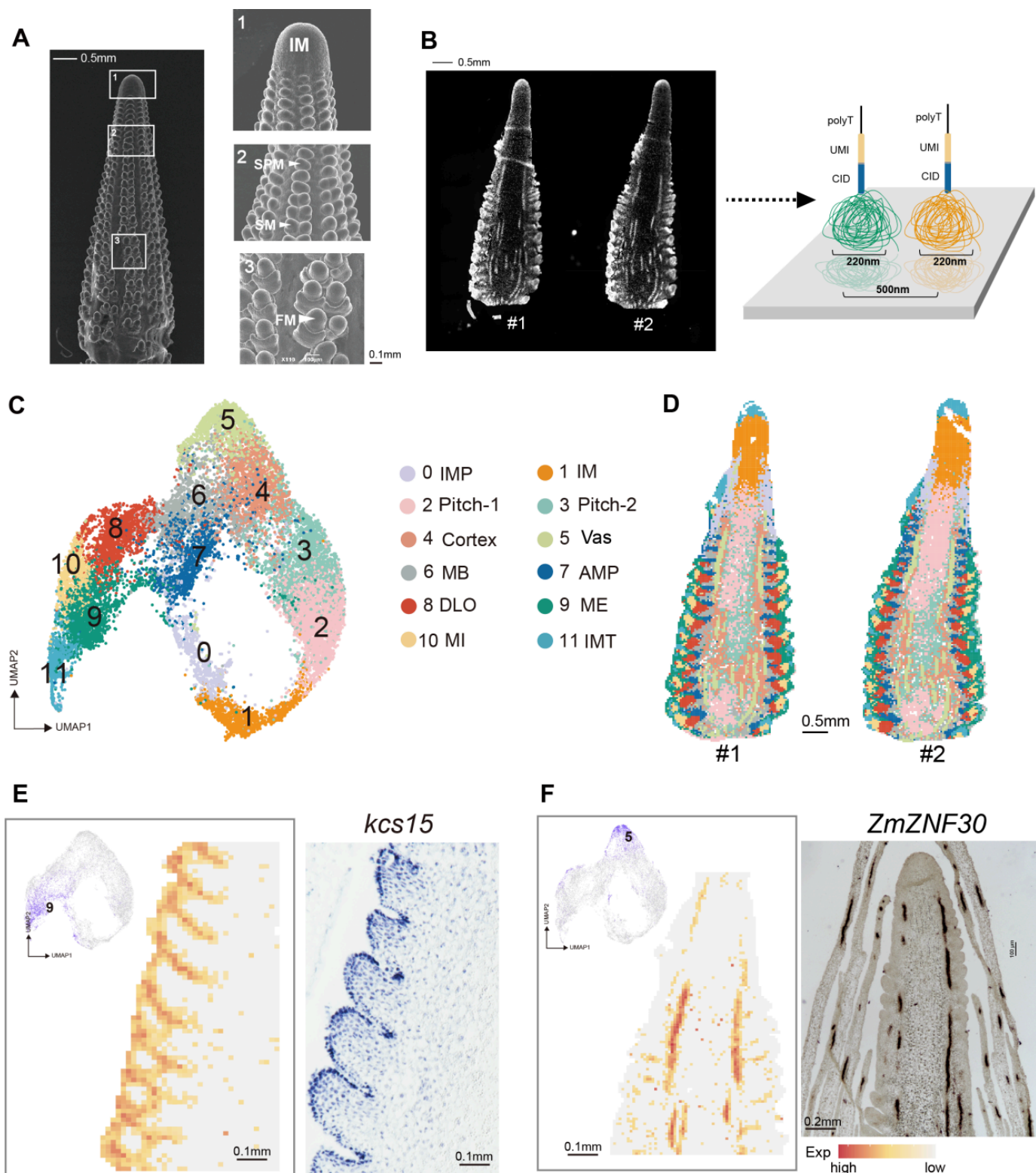


**Figure 1**

**A spatial transcriptomic atlas of the maize developing ear.**

**(A)** Left, a scanning electron microscope image of a maize developing ear (scale bar=0.5mm). Right, close-ups of inflorescence meristem (IM), spikelet pair meristems (SPM), spikelet meristems (SM), and floral meristems (FM). Scale bar in 1, 2, 3 on the right (scale bar=0.1mm)

**(B)** Nucleic-acid dye staining of a maize 6mm developing ear section attached on a 1-cm<sup>2</sup> chip (left). Scale bar=0.5mm. Stereo-seq process diagram (right): the enlarged image shows the size of each spot and the distance between 2 adjacent spots.

**(C)** Twelve clusters are displayed by an integrated uniform manifold approximation and projection (UMAP) plot in two dimensions. Each dot representing a bin50 from section #1 and #2.

**(D)** Spatial distribution of cell types that identified in sections #1 and #2. IMP, inflorescence meristem periphery; IM, inflorescence meristem; Vas, Vasculature (xylem, phloem, bundle sheath); MB, meristem base; AMP, adaxial meristem periphery; DLO, determinate lateral organs; ME, meristem epidermis; MI, meristem internal; IMT, inflorescence meristem tip. Scale bar=0.5mm.

**(E)** mRNA *in situ* hybridization of *kcs15* (*3-ketoacyl-CoA synthase15*) validates the Stereo-seq cluster9, meristem epidermis.

**(F)** mRNA *in situ* hybridization of *ZmZNF30* (Zinc Finger Protein 30) validates the Stereo-seq cluster5, vasculature. *ZmZNF30* was also validated as marker gene for phloem (Xu et al., 2021).

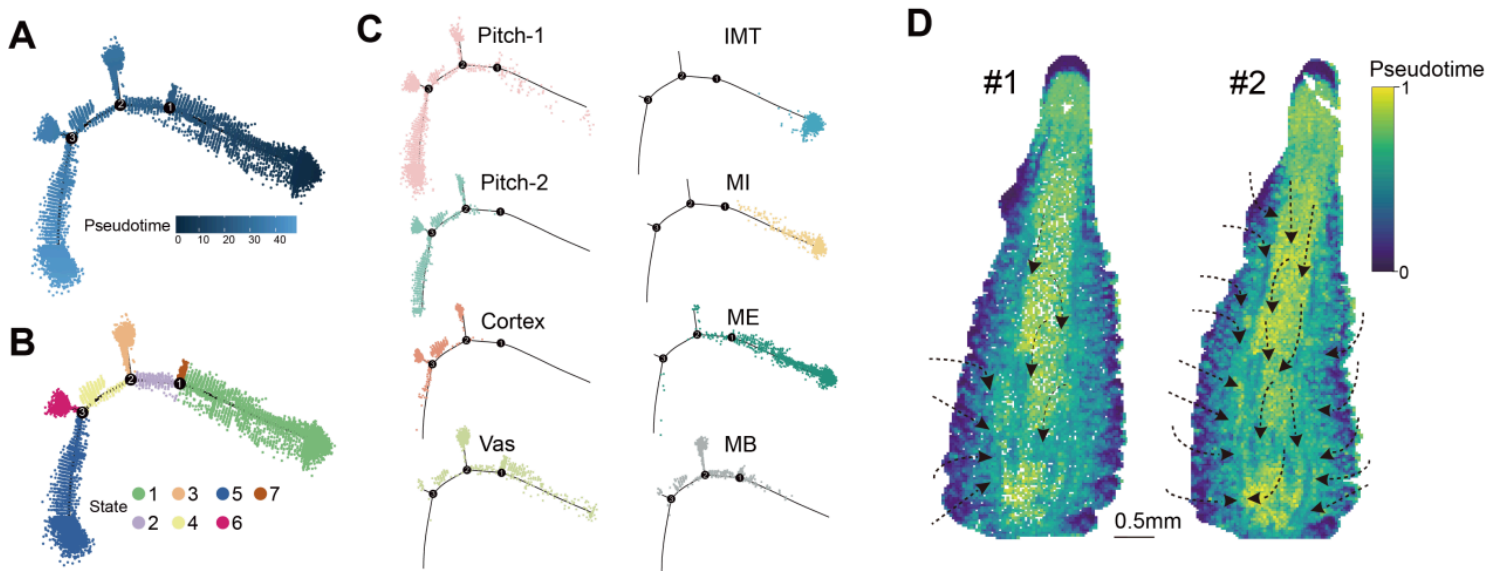


**Figure 2**

### Developmental trajectories of maize 6mm ear

**(A)** Pseudotime analysis using bin50s of #1 and #2 sections.

**(B)** Pseudotime stages of bin50s of #1 and #2 sections.

**(C)** Distribution of bin50s that are mainly located in cob and floret on the pseudotime trajectory branches.

**(D)** RNA velocity analysis showing the predicted trajectory of maize 6mm ear. Bin50s are colored by the vector field-based pseudotime score. and positioned in the same coordinates as in Figure 1D. Scale bar=0.5mm.

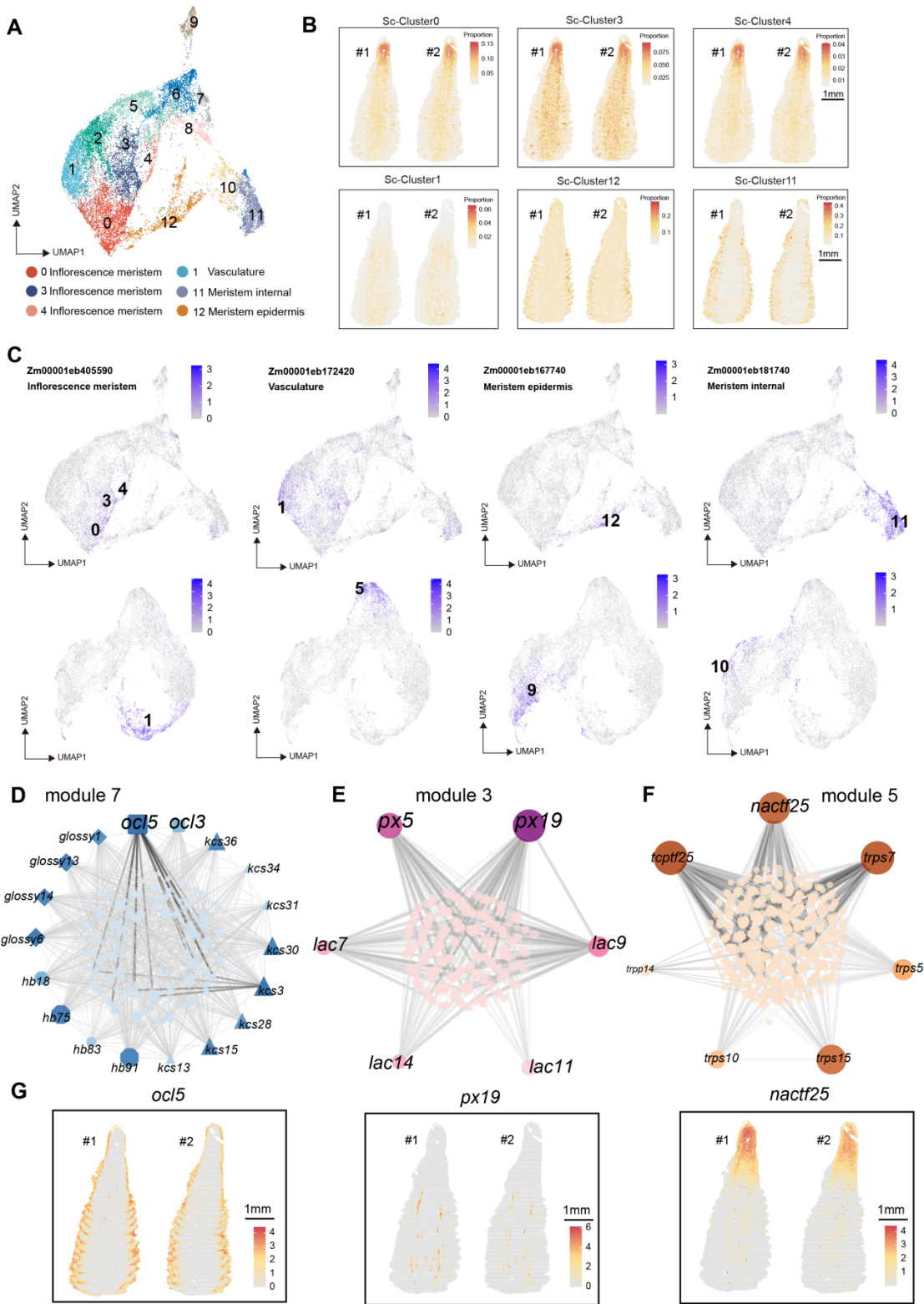


**Figure 3**

**Constructing spatial co-expression networks by integrating scRNA-seq and Stereo-seq.**

(A) Thirteen clusters visualized by an integrated uniform manifold approximation and projection (UMAP) plot in, with each dot representing a cell.

(B) The proportion of cells from different Sc-clusters in the spots. Scale bar=1mm.



**(C)** Top, UMAP plots of marker genes, the numbers in the figures indicate that the gene is the marker gene of the corresponding Sc-cluster, with color scale indicating normalized expression level in scRNA-seq. Bottom, UMAP plots of the same genes, the numbers in the figures indicate that the gene is the marker gene of the corresponding cluster, with color scale indicating normalized expression level in Stereo-seq of #1 and #2 sections.

**(D-F)** Co-expression network of gene module3 (D), 5 (E) and 7 (F). The network is visualized by Cytoscape. Node size represents the relative connectivity, The shade of the line color represents the weight of the edge between two nodes.

**(G)** Spatial visualization of three hub genes of module3, 5 and 7 on #1 and #2 section, with color scale indicating normalized expression level in Stereo-seq. Scale bar=1mm.

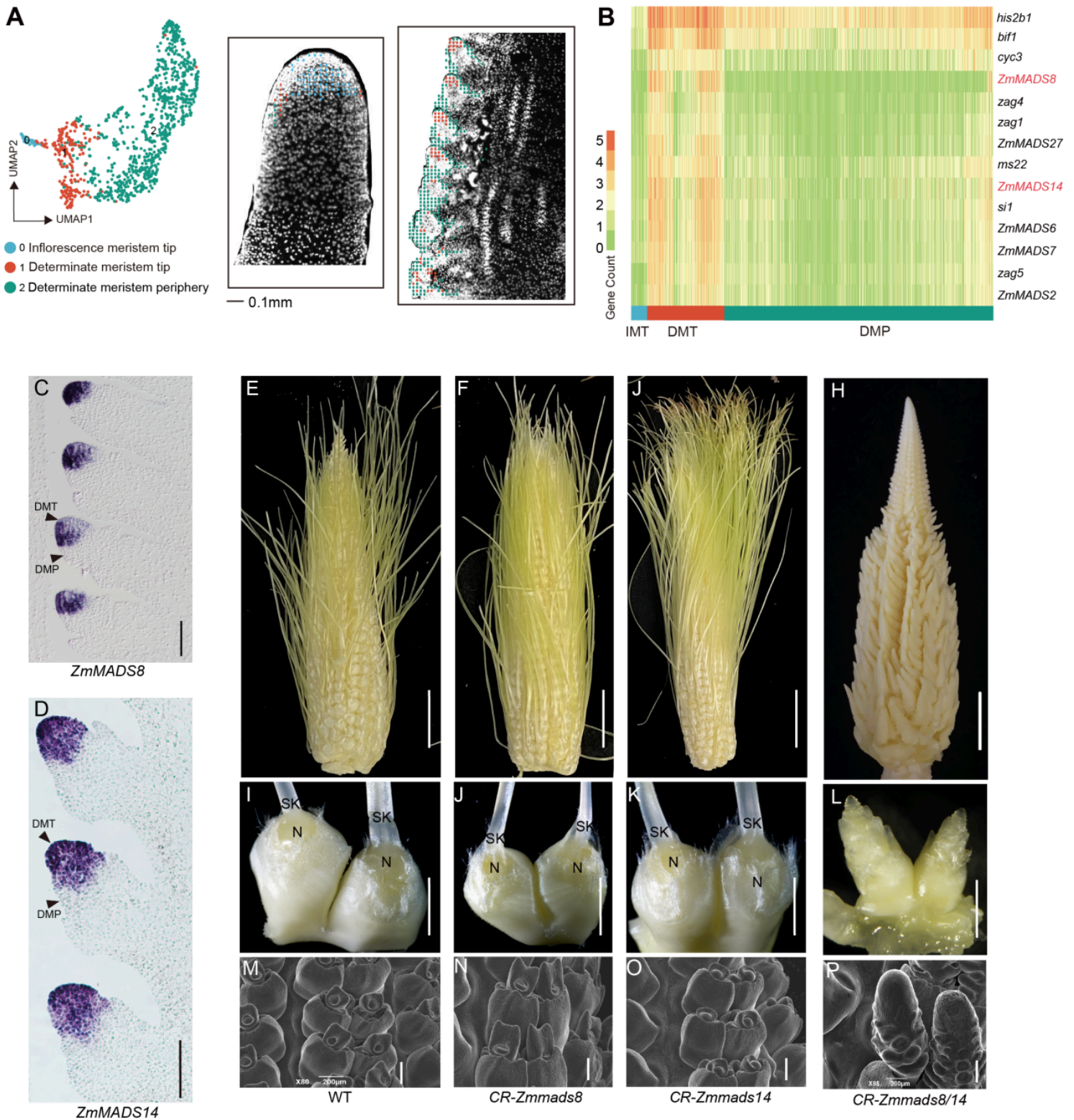


**Figure 4**

*ZmMADS8* and *ZmMADS14* contribute to stem cell differentiation were identified through Stereo-seq data.

(A) Left, Stereo-seq enables the extraction of bin50s distributed in the meristem epidermis and the inflorescence meristem tip. UMAP plot displayed there 3 sub-clusters. Right, physical distribution of bin50s of 3 sub-cluster on #1 sections. Scale bar=0.1mm.



**(B)** Heatmap shows the mean expression level of the 14 genes involved in maize ear development and is highly expressed in determinate meristem tip. *ZmMADS8* and *ZmMADS14* are highlighted by red color. IMT, inflorescence meristem tip; DMT, determinate meristem tip; DMP, determinate meristem periphery.

**(C-D)** mRNA *in situ* hybridization with antisense probes of *ZmMADS8* (C) and *ZmMADS14* (D). Arrows point out the DMT and DMP, respectively. Scale bar = 0.1 mm.

**(E-H)** The ear phenotypes of wild-type (E), *CR-Zmmads8* (F), *CR-Zmmads14* (J) and *CR-Zmmads8/14* (H). Scale bar = 2 cm.

**(I-L)** The female flower phenotypes of wild-type (I), *CR-Zmmads8* (J), *CR-Zmmads14* (K) and *CR-Zmmads8/14* (L). SK, silk; N, nucellus. Scale bar = 0.5 cm.

**(M-P)** Scanning electron microscope images of the Floret meristem in wild-type (M), *CR-Zmmads8* (N), *CR-Zmmads14* (O) and *CR-Zmmads8/14* (P). Scale bar = 0.2 mm.

## Supplementary Files

This is a list of supplementary files associated with this preprint. Click to download.

- [Supplementalwithlegend12wybclean.docx](#)
- [SupplementaryData1mRNAinsituhybridizationresult.docx](#)
- [SupplementaryTable1Basicdatastatisticsofmaizeearsinglecellandspatialtranscriptomesequencing.xlsx](#)
- [SupplementaryTable10TheproportionofcellsfromdifferentScclustersinthepotsofsectionX4.xlsx](#)
- [SupplementaryTable2ClusterspecificmarkergenesidentifiedinStereoSeqdata.xlsx](#)
- [SupplementaryTable3ClusterspecificmarkergenesidentifiedinScRNAseqdata.xlsx](#)
- [SupplementaryTable4Identificationof12genecoexpressionmodulesusingScRNAseq.xlsx](#)
- [SupplementaryTable5Hubgenesheritability.xlsx](#)
- [SupplementaryTable6ClusterspecificmarkergenesforIMTandMEcells.xlsx](#)
- [SupplementaryTable7PrimersandprobesusedinresequencingandmRNAinsituexperiments.xlsx](#)
- [SupplementaryTable8TheproportionofcellsfromdifferentScclustersinthepotsofsectionX1andX2.xlsx](#)
- [SupplementaryTable9TheproportionofcellsfromdifferentScclustersinthepotsofsectionX3.xlsx](#)